Nucleon to Δ transition form factors with $N_F = 2 + 1$ domain wall fermions

C. Alexandrou[(a,b)], G. Koutsou[(c)], J. W. Negele[(d)], Y. Proestos[(b)] and A. Tsapalis[(e,f)]

[(a)] *Department of Physics, University of Cyprus, P.O. Box 20537, 1678 Nicosia, Cyprus*

[(b)] *Computation-based Science and Technology Research Center, The Cyprus Institute, P.O. Box 27456, 1645 Nicosia, Cyprus*

[(c)] *Department of Physics, University of Wuppertal/Forschungszentrum Jülich D-52425, Jülich, Germany*

[(d)] *Center for Theoretical Physics, Laboratory for Nuclear Science and Department of Physics, Massachusetts Institute of Technology, Cambridge, Massachusetts 02139, U.S.A.*

[(e)] *Hellenic Naval Academy, Hatzikyriakou Ave., Pireaus 18539, Greece*

[(f)] *Department of Physics, National Technical University of Athens, Zografou Campus 15780, Athens, Greece*

We calculate the electromagnetic, axial and pseudo-scalar form factors of the Nucleon to $\Delta(1232)$ transition using two dynamical light degenerate quarks and a dynamical strange quark simulated with the domain wall fermion action. Results are obtained at lattice spacings $a = 0.114$ fm and $a = 0.084$ fm, with corresponding pion masses of 330 MeV and 297 MeV, respectively. High statistics measurements are achieved by utilizing the coherent sink technique. The dominant electromagnetic dipole form factor, the axial form factors and the pseudo-scalar coupling are extracted to a good accuracy. This allows the investigation of the non-diagonal Goldberger-Treiman relation. Particular emphasis is given on the extraction of the sub-dominant electromagnetic quadrupole form factors and their ratio to the dominant dipole form factor, R_{EM} and R_{SM}, measured in experiment.

PACS numbers: 11.15.Ha, 12.38.Gc, 12.38.Aw, 12.38.-t, 14.70.Dj

I. INTRODUCTION

Form factors are fundamental quantities which probe the internal structure of the hadron. They are typically extracted from electromagnetic or weak scattering processes on hadronic targets, dominated by one-body exchange currents. The prime example are the form factors of the proton, which remain the most well-studied. Its electromagnetic (Sachs) form factors have been measured since the 50's [1] and static properties such as the magnetic moment and the charge radius are extracted. For recent reviews on the experimental and theoretical status we refer the reader to Refs. [1, 2] and [3, 4] respectively. Despite the long history of measurements of the electromagnetic nucleon form factors, polarization experiments recently revealed an unexpected behaviour in the momentum dependence of the electric to magnetic form factor of the proton which has triggered

theoretical investigations to explain the dynamics that give rise to such behavior [5].

The proton, being the building block of all matter that is presently observed to be stable, provides a nice laboratory for studying a relativistic bound state. One fundamental question is whether hadrons being composite systems are deformed and in particular whether the proton is spherical or has an intrinsic deformation. The elastic form factors do not suffice to answer this question on nucleon deformation, an important quantity that characterizes the distribution of quarks in the nucleon. The reason lies in the fact that the spectroscopic quadrupole moment of an $J = 1/2$ state vanishes identically in the laboratory frame if a one-photon exchange process is studied, although a quadrupole deformation may still exist in the body-fixed intrinsic frame. Therefore, regarding the nucleon, one has to study the transition to the lowest positive parity $J = 3/2$ state which is the $\Delta(1232)$. The $\gamma N\Delta$ matrix element is parameterized in terms of a dominant magnetic dipole, G_{M1}, plus the sub-dominant electric quadrupole, G_{E2}, and Coulomb quadrupole, G_{C2}, transition form factors. Detection of non-zero G_{E2} or G_{C2} signals the existence of deformation in the $N-\Delta$ system [6–8]. Precise electroproduction experiments in the last decade demonstrated that this is indeed the case and provided measurements of the EM transition form factors for a wide range of values of the momentum transfer squared q^2. The $E2$ and $C2$ amplitudes are measured to a few percent of the dominant, $M1$, amplitude and are typically given as ratios to the $M1$ amplitude, denoted by R_{EM} and R_{SM} respectively.

State-of-the-art lattice QCD calculations can yield model independent results on hadron form factors, thereby providing direct comparison with experiment. Like in experiment, the electromagnetic nucleon form factors have been studied by many collaborations recently using dynamical simulations [9–15]. Reproducing the experimental results on the electric and magnetic form factors is a prerequisite for enabling lattice predictions of other form factors. This is also true for lattice calculations of the dominant magnetic dipole N to Δ transition form factor which is also well measured experimentally. In particular, in the case of the N to Δ, there are no disconnected contributions and therefore reproducing this form factor would provide a validation of lattice QCD techniques in calculating hadron form factors. The evaluation of the sub-dominant N to Δ electric and Coulomb quadrupole form factors have also been studied for many years in dedicated experiments since, as we already pointed out, a non-zero value of these form factors signals a deformation in the N-Δ system. However the experimental determination needs model input and therefore lattice QCD can provide an ab initio calculation of these fundamental quantities.

In the axial sector, in the case of the nucleon, there exist two form factors, the axial, G_A, and induced pseudo-scalar, G_p, form factors. They have been studied in neutrino scattering and muon

capture experiments, respectively but experimental data are less precise [16, 17]. There have also been several lattice evaluations of the nucleon axial charge g_A [9, 18–20] and of the momentum dependence of the two form factors [12, 21]. Partial conservation of axial symmetry (PCAC) leads to a relation between the nucleon axial charge and the pseudo-scalar $\pi - N$ coupling constant $g_{\pi NN}$, the well-known Goldberger-Treiman relation. The strong decay of the Δ obscures greatly experimental studies of the N to Δ weak matrix element but some information on the dominant axial transition form factors $C_5^A(q^2)$ and $C_6^A(q^2)$ is available from neutrino interactions on hydrogen and deuterium targets. C_5^A and C_6^A are the analogue of the nucleon axial form factors, G_A and G_p, respectively. Indeed, like G_p, the q^2 dependence of C_6^A is dominated by the pion pole and due to the axial Ward-Takahashi identity (AWI) a relation can be derived between C_5^A and the phenomenological strong coupling of the pion-nucleon-Δ vertex, $g_{\pi N\Delta}$. This relation is referred to as the non-diagonal Goldberger-Treiman relation.

Such observations strongly motivate the study of the N-to-Δ transition from first principles using lattice QCD. The first lattice study of the electromagnetic $\gamma N\Delta$ transition was carried out in the quenched approximation [22] at a fixed Euclidean momentum transfer squared $Q^2 = -q^2$ with inconclusive results as to whether the $E2$ or $C2$ amplitudes were non-zero due to large statistical errors. A study employing the formalism of Ref. [22] followed using quenched and two dynamical flavors of degenerate Wilson-type quarks at smaller quark masses but still only at the lowest q^2-value allowed on the lattices at hand. Although there was an almost ten-fold increase in statistics the values obtained for the quadrupole form factors had large statistical noise and a zero value could not be excluded [23, 24]. In order to obtain sufficient accuracy we combined sequential inversions through the source instead of through the current for the evaluation of the three-point functions and optimized sources that led to a large sample of statistically independent measurements for a given q^2-value. The calculation, carried out in the quenched approximation, confirmed a non-zero value with the correct sign for both of the quadrupole amplitudes [25, 26]. A similar study was also carried out for the axial vector N to Δ matrix element [27]. Using this new methodology we extended the calculation of the N to Δ electro-weak form factors to unquenched lattice QCD. For the latter study we used $N_f = 2$ Wilson fermions as well as an $N_f = 2 + 1$ calculation with a mixed action with domain wall valence quarks on a staggered sea reaching a pion mass of about 350 MeV [21, 28–30]. This calculation showed that the unquenched results on the Coulomb quadrupole form factor at low q^2 decreased towards the experimental results. However, the discrepancy in the momentum dependence of the dominant dipole form factor remained with lattice results having smaller values at low q^2-values and a weaker dependence on q^2. Using the same set of sequential

propogators as in the electromagnetic case the axial and pseudo-scalar N to Δ form factors were studied [21, 30]. The strong coupling constant $g_{\pi N\Delta}$ and non-diagonal Goldberger-Treiman relation were examined in detail and it was demonstrated that the behaviour is very similar manner to the corresponding relations in the nucleon system.

In this work we study the N-to-Δ transition using $N_F = 2+1$ dynamical domain wall fermions simulated by the RBC-UKQCD collaborations [31]. This eliminates ambiguities about the correctness of the continuum limit due to the rooting of the staggered sea quarks and the matching required in a mixed action. Preliminary results have been presented in Refs. [32]. We use two ensembles corresponding to lattice spacing $a = 0.114$ fm and $a = 0.084$ fm and physical volume of $(2.7 \text{ fm})^3$. Both lattice spacings are smaller than the lattice spacing used in our previous mixed-action calculation. This allows, for the first time, the investigation of cut-off effects on these hadronic observables. For each lattice spacing, we chose to perform the calculation on the lightest pion mass set available, namely at 330 MeV pions for the coarse lattice and 297 MeV for the fine one, in order to be as close as possible to the physical regime. The goal is, first, to check whether lattice results on the well measured experimentally dominant dipole form approach experiment. Secondly, we would like to see the onset of the large pion cloud contributions to the quadrupole form factors as predicted by chiral effective theory [33]. Thirdly we will extract the axial N to Δ coupling that enters in chiral expansions of the nucleon axial charge as well as the strong coupling constant $g_{\pi N\Delta}$. Determining these quantities together with the corresponding quantities g_A and $g_{\pi NN}$ for the nucleon as well as for the Δ on the same gauge configurations will enable simultaneous chiral extrapolations to the physical point and yield more reliable results on these fundamental quantities.

The paper is organized as follows: In Section II we describe the general lattice setup and outline the techniques utilized to extract all the transition form factors from three-point functions measured on the lattice. In Section III we present in detail the decomposition of the electromagnetic N to Δ matrix element on the hadronic level in terms of the Sachs form factors and discuss the results for the electromagnetic transition form factors. In Section IV we give the corresponding matrix element for the electro-weak transition and discuss the results on the axial and pseudo-scalar form factors. Finally, the last section contains our conclusions and an outlook regarding further studies in the subject.

II. LATTICE SETUP AND TECHNIQUES

We use the $N_f = 2 + 1$ dynamical domain wall fermion (DWF) ensembles generated by the RBC and UKQCD collaborations [31, 34, 35] with the strange quark mass fixed at the physical point. Specifically, we consider gauge configurations on lattices of volume $24^3 \times 64$ corresponding to a pion mass of about 330 MeV and inverse lattice spacing $a^{-1} = 1.73(3)$ GeV and $32^3 \times 64$ corresponding to a pion mass of about 297 MeV and $a^{-1} = 2.34(3)$ GeV. We refer to the former lattice corresponding to $a^{-1} = 1.73(3)$ GeV, as the *coarse* DWF lattice, and the one corresponding to $a^{-1} = 2.34(3)$ GeV, as the *fine* DWF lattice.

Domain wall fermions preserve chiral symmetry in the infinite limit of the fifth dimension, L_5. In actual computations L_5 is finite leading to an additive contribution to the quark mass as defined through the Axial Ward-Takahashi Identity (AWI). For the coarse ensemble a residual quark mass of $am_{res} = 0.00315(2)$ has been measured by UKQCD-RBC [31] with the extent of the fifth dimension set to $L_5 = 16$. The same L_5 extent for the fine ensemble leads to a much smaller violation, measured to $am_{res} = 0.000665(3)$, or just 17% of the bare quark mass [11].

Details about the lattice parameters used in this study are provided in Table I, where for comparison the relevant values of the parameters used in our previous study using the mixed action [12, 21, 28] are also given.

Volume	$N_{\text{confs}}^{\text{dom.}}$ ($N_{\text{meas.}}$)	$N_{\text{confs}}^{\text{subd.}}$ ($N_{\text{meas.}}$)	a^{-1} [GeV]	Z_V	Z_A	$m_{u,d}/m_s$	m_π [GeV]	m_N [GeV]	m_Δ [GeV]
coarse $N_F = 2 + 1$ DWF [31]									
$24^3 \times 64$	200 (800)	398 (1592)	1.73(3)	0.7161(1)	0.7161(1)	0.005/0.04	0.329(1)	1.130(6)	1.457(11)
fine $N_F = 2 + 1$ DWF [11]									
$32^3 \times 64$	176 (704)	309 (1236)	2.34(3)	0.7468(39)	0.74521(2)	0.004/0.03	0.297(5)	1.127(9)	1.455(17)
Hybrid action [12]									
DWF valence: $am_{u,d} = 0.0138$, $am_s = 0.081$									
$28^3 \times 64$	300 (300)	300 (300)	1.58(3)			0.01/0.05	0.353(2)	1.191(19)	1.533(27)

TABLE I: Parameters for the calculation of the electromagnetic and axial transition form factors. The mixed action results from Refs. [21, 28] are also included for completeness. In the second (third) column we show the number of gauge configurations used for the dominant (suppressed) form factors. For the DWF lattices the numbers in the parentheses next to the number of configurations are multiplied by four, since the coherent sink method was employed, showing the actual number of measurements taken into account in the overconstrained analysis. In the fifth and sixth columns we list the values of the vector and axial current renormalization constants, respectively that have been used as input parameters in our calculation, since we have used local currents and not the lattice conserved ones.

In order to create the proton and Δ^+ states we use the standard interpolating operators

$$\chi^p(x) = \epsilon^{abc} \left[u^{T\,a}(x)\, C\gamma_5 d^b(x)\right] u^c(x), \tag{1}$$

$$\chi^{\Delta^+}_\sigma(x) = \frac{1}{\sqrt{3}}\epsilon^{abc}\Big\{2\left[u^{Ta}(x)\, C\gamma_\sigma d^b(x)\right] u^c(x) + \left[u^{Ta}(x)\, C\gamma_\sigma u^b(x)\right] d^c(x)\Big\}, \tag{2}$$

respectively. The $J = 3/2$ Δ state is described by the Rarita-Schwinger vector-spinor where $\sigma = 1, 2, 3, 4$ is the Lorentz vector field index. $C = \gamma_4\gamma_2$ is the charge-conjugation matrix.

Form factors of the $N - \Delta$ transition are extracted on the lattice from the three-point function

$$\langle G^{\Delta J_\mu N}_\sigma(t_2, t_1; \mathbf{p}\,', \mathbf{p}; \Gamma_\tau)\rangle = \sum_{\mathbf{x}_2,\, \mathbf{x}_1} e^{-i\mathbf{p}'\cdot\mathbf{x}_2} e^{+i\mathbf{q}\cdot\mathbf{x}_1}\, \Gamma^{\beta\alpha}_\tau \langle\Omega|T\left[\chi^{\sigma\alpha}_\Delta(\mathbf{x}_2, t_2) J_\mu(\mathbf{x}_1, t_1)\bar{\chi}^\beta_N(\mathbf{0}, 0)\right]|\Omega\rangle \tag{3}$$

In this notation, an initial nucleon state with momentum $\mathbf{p}$ is created at time zero and propagated to a later time t_1 at which it couples to the current J causing a transition to the Δ state of momentum $\mathbf{p}'$ which is annihilated at a later time t_2. $\mathbf{q} = \mathbf{p}' - \mathbf{p}$ is the momentum transfer. The projection matrices Γ_τ are given by

$$\Gamma_i = \frac{1}{2}\begin{pmatrix} \sigma_i & 0 \\ 0 & 0 \end{pmatrix}, \quad \Gamma_4 = \frac{1}{2}\begin{pmatrix} \mathbb{1} & 0 \\ 0 & 0 \end{pmatrix}. \tag{4}$$

The one-body currents considered in this work include the local vector current

$$V_\mu(x) = \frac{2}{3}\bar{u}(x)\gamma_\mu u(x) - \frac{1}{3}\bar{d}(x)\gamma_\mu d(x) \quad , \tag{5}$$

the axial-vector current and pseudo-scalar density

$$A^a_\mu(x) = \bar{\psi}(x)\gamma_\mu\gamma_5\frac{\tau^a}{2}\psi(x) \quad , \quad P^a(x) = \bar{\psi}(x)\gamma_5\frac{\tau^a}{2}\psi(x) \tag{6}$$

with τ^a the three Pauli-matrices acting in flavor space and ψ the isospin doublet quark field. Note that due to the $\Delta J = 1$ nature of the transition, only the isovector part of V_μ contributes and, due to isospin symmetry, only the flavor diagonal operator τ^3 needs to be evaluated. Inclusion of baryon states in the three-point function (3) and the use of standard Euclidean spin-sums for the Rarita-Schwinger field

$$\sum_s u_\sigma(p, s)\bar{u}_\tau(p, s) = \frac{-i\gamma\cdot p + m_\Delta}{2m_\Delta}\left[\delta_{\sigma\,\tau} + \frac{2p_\sigma p_\tau}{3m^2_\Delta} - i\frac{p_\sigma\gamma_\tau - p_\tau\gamma_\sigma}{3m_\Delta} - \frac{1}{3}\gamma_\sigma\gamma_\tau\right], \tag{7}$$

and the Dirac spinor

$$\sum_s u(p, s)\bar{u}(p, s) = \frac{-i\gamma\cdot p + m_N}{2m_N} \tag{8}$$

lead to the isolation of the desired matrix element, assuming that the initial and final ground states dominate the propagation before and after the operator insertion, respectively. In order to cancel, in the large Euclidean time limit, the dependence on the Euclidean time evolution and on the unknown overlaps of the nucleon and Δ states with the initial states, we form the following ratio:

$$R^J_\sigma(t_2,t_1;\mathbf{p}\,',\mathbf{p}\,;\Gamma_\tau;\mu) = \frac{\langle G^{\Delta J_\mu N}_\sigma(t_2,t_1;\mathbf{p}\,',\mathbf{p};\Gamma)\rangle}{\langle G^{\Delta\Delta}_{ii}(t_2,\mathbf{p}\,';\Gamma_4)\rangle} \times\left[\frac{\langle G^{\Delta\Delta}_{ii}(t_2,\mathbf{p}\,';\Gamma_4)\rangle}{\langle G^{NN}(t_2,\mathbf{p};\Gamma_4)\rangle}\,\frac{\langle G^{NN}(t_2-t_1,\mathbf{p};\Gamma_4)\rangle\,\langle G^{\Delta\Delta}_{ii}(t_1,\mathbf{p}\,';\Gamma_4)\rangle}{\langle G^{\Delta\Delta}_{ii}(t_2-t_1,\mathbf{p}\,';\Gamma_4)\rangle\,\langle G^{NN}(t_1,\mathbf{p};\Gamma_4)\rangle}\right]^{1/2} \tag{9}$$

which requires also measurements of the nucleon (G^{NN}) and Δ ($G^{\Delta\Delta}_{\sigma\tau}$) two-point functions

$$\langle G^{NN}(t,\mathbf{p};\Gamma)\rangle = \sum_{\mathbf{x}} e^{-i\mathbf{p}\cdot\mathbf{x}}\,\Gamma^{\beta\alpha}\,\langle\Omega|\,T\,\chi^\alpha(\mathbf{x},t)\bar\chi^\beta(\mathbf{0},0)\,|\Omega\,\rangle, \tag{10}$$

$$\langle G^{\Delta\Delta}_{\sigma\tau}(t,\mathbf{p};\Gamma)\rangle = \sum_{\mathbf{x}} e^{-i\mathbf{p}\cdot\mathbf{x}}\,\Gamma^{\beta\alpha}\,\langle\Omega|\,T\,\chi^\alpha_\sigma(\mathbf{x},t)\bar\chi^\beta_\tau(\mathbf{0},0)\,|\Omega\,\rangle. \tag{11}$$

Implicit summations on indices $i=1,2,3$ are assumed in the above ratio (9), which is designed such that the time evolution (and consequently the noise) appearing in its two-point function part is minimized. In the large Euclidean time limit ($t_2-t_1\gg 1,\ t_1\gg 1$) where we have ground state dominance this ratio (9) thus yields a a time-independent function $\Pi^J_\sigma(\mathbf{p}\,',\mathbf{p}\,;\Gamma_\tau;\mu)$ that is related to the matrix element $\langle\Delta(\mathbf{p}')|J|n(\mathbf{p})\rangle$. Therefore we look for the plateau region of Eq. (9) in order to extract the matrix element that we are interested in. For a given operator insertion J and projection matrix Γ_τ, the function $\Pi^J_\sigma(\mathbf{p}\,',\mathbf{p}\,;\Gamma_\tau;\mu)$ is a linear combination of the corresponding form factors. These relations for the appropriate choice of Γ_τ and Δ vector index σ will be given in the following sections.

The computationally intensive part of the calculation lies in the calculation of the three-point function given in Eq. (3). In order to achieve the extraction of the momentum dependence of the matrix element for the $V_\mu(x)$, $A^3_\mu(x)$ and $P^3(x)$ insertions, one needs an evaluation for a large number of values of the momentum transfer $\mathbf{q}$. This is feasible by evaluating the matrix element using *sequential inversions through the sink*. In this method, the quantum numbers of the source and sink interpolating fields are fixed, effectively by fixing the σ and τ indices. The time slices of the source and sink are, in addition, fixed. The quark propagator with the operator insertion is obtained by the joining of a forward propagator and the *sequential propagator* which is obtained by using as a source the baryon state at the sink folded in with the two forward propagators from the source. With the forward and sequential propagators available, the operator insertion at selected intermediate times t_1 and momenta transfers $\mathbf{q}$ is readily available. In this method the final state, in this case the Δ-state, is always at rest. Since the $\sigma-\tau$ space of indices still spans

a set of 16 independent inversions that would be required, an optimization in this space has been exploited. Three linear combinations are constructed from which the EM, axial and pseudo-scalar form factors are extracted such that the maximal set of statistically independent measurements of momentum transfer vectors $\mathbf{q}$ per q^2 value is achieved. In addition, they are chosen to decouple the dominant dipole ($M1$) part of the EM transition from the sub-dominant quadrupoles $E2$ and $C2$ measurements. The three linear combinations which we construct and measure in this work are given below.

$$S_1^J(\mathbf{q};J) = \sum_{\sigma=1}^{3} \Pi_\sigma^J(\mathbf{0},-\mathbf{q}\,;\Gamma_4;J) \tag{12}$$

$$S_2^J(\mathbf{q};J) = \sum_{\sigma\neq k=1}^{3} \Pi_\sigma^J(\mathbf{0},-\mathbf{q}\,;\Gamma_k;J) \tag{13}$$

$$S_3^J(\mathbf{q};J) = \Pi_3^J(\mathbf{0},-\mathbf{q}\,;\Gamma_3;J) - \frac{1}{2}\Big[\Pi_1^J(\mathbf{0},-\mathbf{q}\,;\Gamma_1;J) + \Pi_2^J(\mathbf{0},-\mathbf{q}\,;\Gamma_2;J)\Big] \quad , \tag{14}$$

where J denotes the operators V_μ, A_μ^3 and P^3. Occasionally we refer to S_1, S_2, S_3 as *optimal* Δ *sinks*, although they actually correspond to an optimal linear combination of the full $N-\Delta$ three-point function with arbitrary insertion J. We stress that, given the forward propagators, *three* inversions in total are required in order to compute the momentum dependence of the full $N-\Delta$ transition and extract the electromagnetic, axial and pseudo-scalar form factors.

Since the source-sink separation is fixed in this method it is crucial to suppress the excited baryon states as much as possible. This is achieved by employing gauge invariant Gaussian smearing on the local quark fields with APE-smeared gauge fields and parameters that have been carefully optimized for the nucleon state. For the coarse lattice, we show in Fig. 1 a comparison of results obtained with a sink-source separation of 0.91 fm and 1.14 fm. As can be seen, extending the source-sink separation to 1.14 fm, the plateau values for the dominant magnetic dipole form factor G_{M1}, which are the most accurate, are consistent with a time-separation of 0.91 fm. Since the larger time separation introduces a doubling in the statistical noise, for the accuracy needed in this study, we opt to use the smaller sink-source separation in time. For the fine lattice, we take a sink-source separation of $\Delta T = 12a$ corresponding to 1.01 fm, consistent with our findings using the coarse lattice.

In order to improve accuracy, a goal that is particularly crucial for the extraction of the sub-dominant electromagnetic form factors, we employ a new method first implemented in the study of the nucleon form factors [11] and referred to as the *coherent sink technique*. The method consists of creating four sets of forward propagators for each configuration at source positions separated in

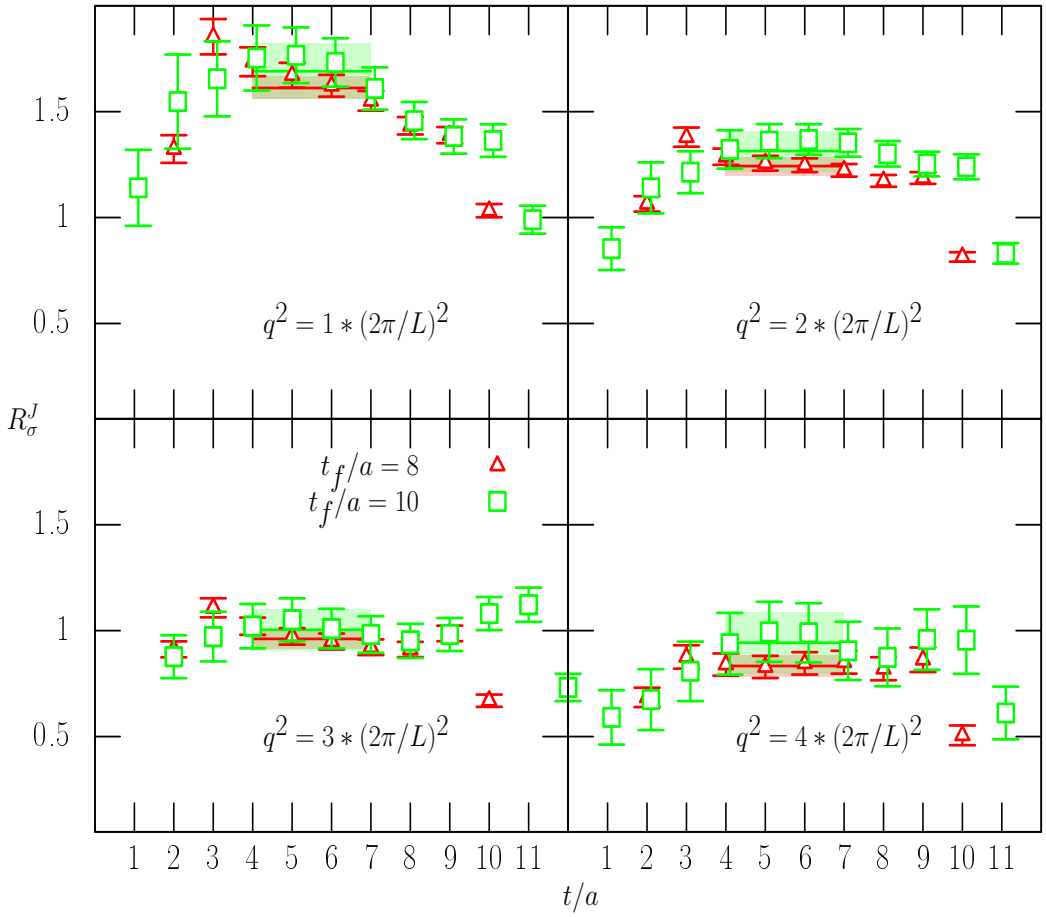

FIG. 1: The ratio R_σ^J from the source S_1 of Eq. (9) versus t/a for a source-sink separation 0.91 fm shifted by a time slice (triangles) and 1.14 fm (squares) for the four smallest non-zero $\vec{q}^2$ values. The fit range is also shown along with the fitted lines and the corresponding error bands. The behavior is the same for both, but the error reduction is better in the former, which is what we therefore utilize in the calculations.

time by one-quarter of the total temporal size. Namely, for the coarse DWF lattice, $N_L = 24$, we have forward propagators generated with sources positioned at:

$$\left\{(\vec{0}, 0),\ (\frac{\vec{L}}{2}, 16a),\ (\frac{\vec{L}}{4}, 32a),\ (\frac{3\vec{L}}{4}, 48a)\right\},$$

and for the fine DWF lattice, $N_L = 32$, placed at:

$$\left\{(\vec{0}, 10a),\ (\frac{\vec{L}}{2}, 26a),\ (\vec{0}, 42a),\ (\frac{\vec{L}}{2}, 58a)\right\},$$

or

$$\left\{(\frac{\vec{L}}{4}, 10a),\ (\frac{3\vec{L}}{4}, 26a),\ (\frac{\vec{L}}{4}, 42a),\ (\frac{3\vec{L}}{4}, 58a)\right\}.$$

From each source $(\vec{x}_i, T_i)$, a zero-momentum projected Δ source is constructed at T_0 slices away, i.e. at $(\vec{x}_i, T_i + T_0)$. For the coarse DWF lattice $T_0/a = 8$, while for the fine DWF lattice

$T_0/a = 12$. Then a *single* coherent backward propagator is calculated in the simultaneous presence of all four sources. The cross terms that arise vanish due to gauge invariance when averaged over the ensemble. The forward propagators have already been computed by the LHPC collaboration [11] and therefore we effectively obtain four measurements at the cost of one sequential inversion. This assumes large enough time-separation between the four sources to suppress contamination among them. A question that arises is whether or not there exist statistically important correlations among these four measurements. In Fig. 2 we show the dependence of the jackknife error on the magnetic dipole G_{M1} for different coherent sink bin sizes. As can be seen, the jackknife errors using one sequential inversion for each are the same as combining all four in single inversion. This is a direct verification that cross-correlations between the different sinks are absent or negligible.

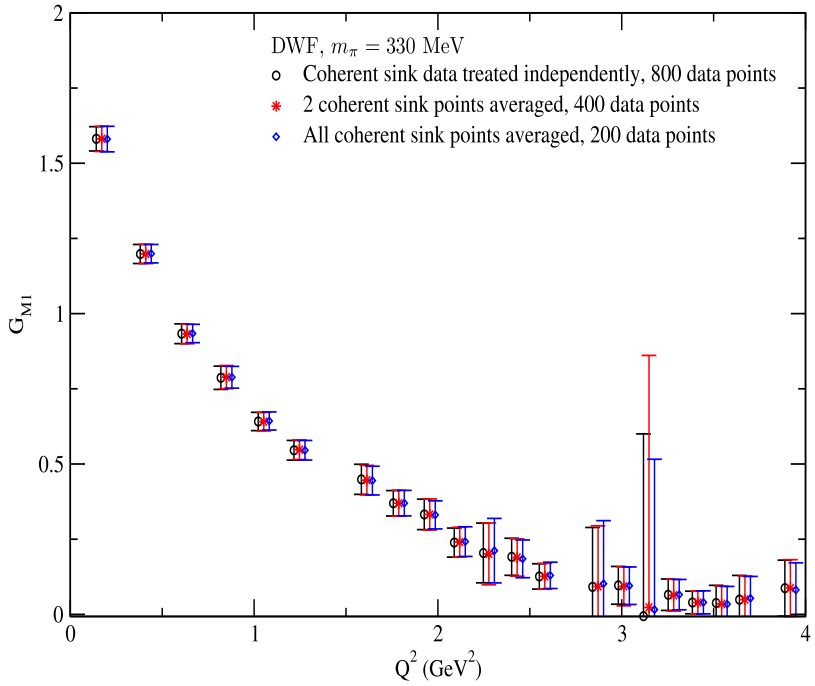

FIG. 2: Dependence of the jackknife error for $G_{M1}(Q^2)$ on the coherent sink bin sizes. This test shows that there is no problem with cross-correlations in the coherent sink method applied in this study.

Finally, the full set of lattice data obtained at a given Q^2 value is analyzed simultaneously by a global χ^2 minimization using the singular value decomposition of an overconstrained linear system [21, 36]. Generically, this consists of setting up the following linear over-complete system of equations

$$P(\mathbf{q};\mu) = D(\mathbf{q};\mu) \cdot F(Q^2), \tag{15}$$

where $P(\mathbf{q};\mu)$ represent the lattice measurements of the appropriately defined ratios of Eq. 9, each

one with its associated statistical weight w_k. The column vector $F(Q^2)$ contains the number M of form factors to be extracted. If we let N represent the number of momentum vectors $\mathbf{q}$ and current directions μ that contribute to a specific value of Q^2, then $D(\mathbf{q};\mu)$ is a matrix structure of the form $N \times M$ which depends on kinematical form factors obtained from the trace algebra on the employed matrix element. The form factors, at the specific Q^2 value, are then extracted from the minimization of the total χ^2:

$$\chi^2 = \sum_{k=1}^{N} \left(\frac{\sum_{j=1}^{2} D_{kj} F_j - P_k}{w_k} \right)^2 , \tag{16}$$

by applying the singular value decomposition on the $N \times M$, $D(\mathbf{q};\mu)$ matrix. All the errors on the lattice measurements as well as the errors on the form factors are determined from the jackknife procedure.

III. ELECTROMAGNETIC N–TO–Δ TRANSITION FORM FACTORS

A. The electromagnetic matrix element

The electromagnetic transition matrix element

$$\langle \Delta(p',s')|j_\mu|N(p,s)\rangle = i\sqrt{\frac{2}{3}} \left(\frac{m_\Delta\, m_N}{E_\Delta(\mathbf{p}')\, E_N(\mathbf{p})} \right)^{1/2} \bar{u}_\sigma(p',s') \mathcal{O}_{\sigma\mu} u(p,s) \tag{17}$$

is decomposed in terms of three multipole form factors:

$$\mathcal{O}_{\sigma\mu} = G_{M1}(q^2) K^{M1}_{\sigma\mu} + G_{E2}(q^2) K^{E2}_{\sigma\mu} + G_{C2}(q^2) K^{C2}_{\sigma\mu}$$

where the kinematical factors in Euclidean space are given by

$$\begin{aligned}
K^{M1}_{\sigma\mu} &= -\frac{3}{(m_\Delta + m_N)^2 + Q^2} \frac{m_\Delta + m_N}{2m_N} \,\mathrm{i}\, \varepsilon_{\sigma\mu\alpha\beta}\, p^\alpha p'^\beta \,, \\
K^{E2}_{\sigma\mu} &= -K^{M1}_{\sigma\mu} + 6\,\Omega^{-1}(Q^2) \frac{m_\Delta + m_N}{2m_N} 2\,\mathrm{i}\,\gamma_5\, \varepsilon_{\sigma\lambda\alpha\beta}\, p^\alpha p'^\beta \varepsilon_\mu{}^{\lambda\gamma\delta}\, p_\gamma p'_\delta \,, \\
K^{C2}_{\sigma\mu} &= -6\,\Omega^{-1}(q^2) \frac{m_\Delta + m_N}{2m_N} \,\mathrm{i}\,\gamma_5\, q_\sigma \left(q^2 (p+p')_\mu - q\cdot(p+p') q_\mu \right) .
\end{aligned} \tag{18}$$

The $p(s)$ and $p'(s')$ denote initial and final momenta (spins), $q^2 \equiv (p'-p)^2$, and $u_\sigma(p',s')$ is a Rarita-Schwinger vector-spinor. We also define $\Omega(Q^2) = \left[(m_\Delta + m_N)^2 + Q^2\right] \left[(m_\Delta - m_N)^2 + Q^2\right]$, with ($\mathbf{Q} = \mathbf{q}$, $Q_4 = iq^0$), so the lattice momentum transfer gives $Q^2 = -q^2$.

In this work we present results for the dominant magnetic dipole form factor $G_{M1}(q^2)$ as well as the sub-dominant electric $G_{E2}(q^2)$ and Coulomb quadrupole $G_{C2}(q^2)$ form factors. Note that these are all scalar functions depending on the momentum transfer $q^2 = -Q^2$, whereas on the lattice only the space-like q^2 are accessible, thus $Q^2 > 0$.

B. The magnetic dipole form factor

The magnetic dipole form factor is directly evaluated from the optimized linear combination S_1^V with the vector current $V_\mu(x)$ insertion. In the large Euclidean time separation limit with the Δ produced at zero momentum we obtain,

$$S_1^V(\mathbf{q}; V_\mu) = iA\Big\{(p_2 - p_3)\delta_{1,\mu} + (p_3 - p_1)\delta_{2,\mu} + (p_1 - p_2)\delta_{3,\mu}\Big\}G_{M1}(Q^2) \quad . \tag{19}$$

The vector index μ takes spatial values, $\mu = 1, 2, 3$ and A is a kinematical constant,

$$A = \sqrt{\frac{2}{3}}\frac{m_\Delta + m_N}{4m_N E_N}\sqrt{\frac{E_N}{E_N + m_N}} \; . \tag{20}$$

The local vector current of Eq. (5) is not conserved by the lattice action and the renormalization constant Z_V, given in Table I, is used to renormalize the current. Z_V is determined from charge conservation that dictates that the electric nucleon form factor is one at $Q^2 = 0$, namely $Z_V = 1/G_E(0) = 1/F_1(0)$ where F_1 is the Dirac form factor.

In Fig. 3 we show the DWF results for the magnetic dipole form factor G_{M1} at $m_\pi = 330$ MeV on the coarse lattice and at $m_\pi = 297$ MeV on the fine lattice as a function of the momentum transfer Q^2. These are compared with our previous results obtained with a hybrid action approach that uses Asqtad improved staggered fermions generated by the MILC collaboration [37] and domain wall valence quarks [28]. The experimentally available data (for more details see Ref. [28]) are also shown in Fig. 3 showing a discrepancy between lattice results and experiment. Although there is a small decrease in the value of G_{M1} at high Q^2 bringing lattice data closer to experiment, the slope at small Q^2 is still smaller than in experiment. The second observation is that although the hybrid calculation used a lattice spacing about 50% larger than the fine DWF lattice, these data show no significant finite a-effects. Fits to a dipole form, $g_0/(1+Q^2/m_0^2)^2$, as well as to an exponential form $\tilde{g_0}\,\exp(-Q^2/\tilde{m}_0^2)$ are shown for the fine DWF lattice. As can be seen they both provide a good description of the lattice results. A list of the fit parameters for all sets is provided in Table II.

The discrepancy between experiment and lattice results is clearly reflected in the value of the dipole mass of $m_0 = 0.78$ GeV obtained by performing a dipole fit to the experimental data as compared to the m_0 values obtained from the lattice results listed in Table II. The steeper rise of the experimental results on G_{M1} as a function of Q^2 near the origin is indicative of the onset of strong chiral quark effects, or equivalently, the lack of strong pion cloud from the still heavy pion mass lattice ensembles that are utilized. Similar behavior has also been observed in the nucleon electromagnetic form factors studies [10, 11, 13]. The N to Δ transition is particularly clean

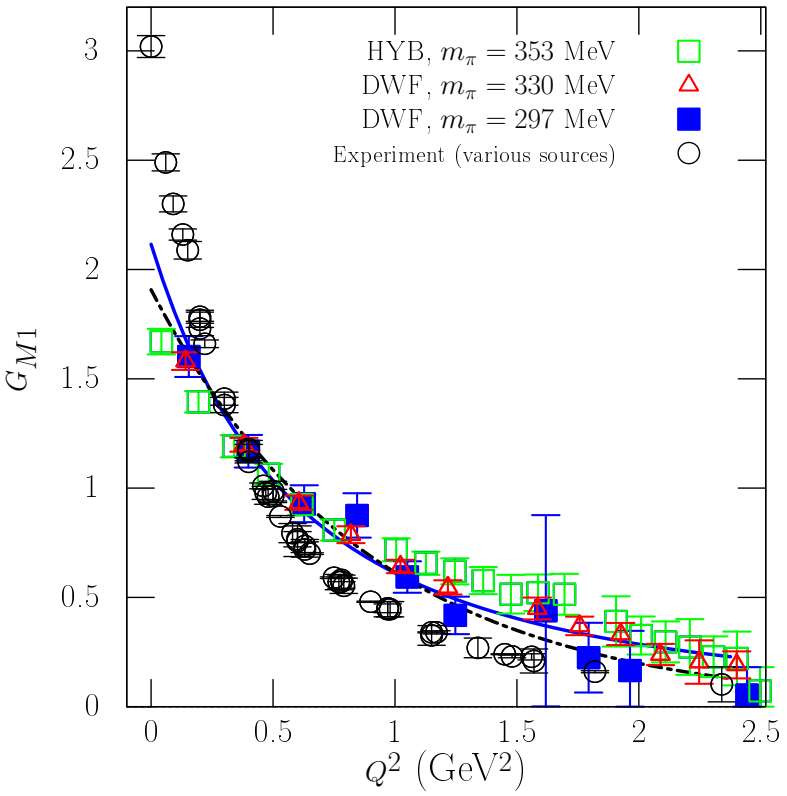

FIG. 3: The magnetic dipole $G_{M1}(Q^2)$ using DWF fermions (both coarse and fine lattices) and using the hybrid action. The circles show the experimental results. The solid blue (dashed black) line is a fit to dipole (exponential) form for the fine DWF lattice.

.

since there is no ambiguity regarding disconnected contributions and thus the flatter dependence observed in the N-to-Δ electromagnetic form factor must be of different origin. Large pion cloud effects would have to set in as we lower the pion mass in order to explain the experimental curve. Such effects have been shown to arise in chiral expansions [33] and it is thus interesting to repeat the calculation for $m_\pi < 250$ MeV where they are expected to become more pronounced.

m_π [GeV]	g_0	m_0 [GeV]	$\tilde{g}_0$	$\tilde{m}_0$ [GeV]
coarse $N_F = 2+1$ DWF				
0.329(1)	1.937(65)	1.171(44)	1.737(53)	1.025(32)
fine $N_F = 2+1$ DWF				
0.297(5)	2.115(161)	1.078(79)	1.907(127)	0.939(55)
HYBRID				
0.353(2)	3.263(64)	1.305(27)	3.05935(61)	1.097(21)
Experiment- (various sources)				
–	3.266(40)	0.745(4)	2.202(67)	0.776(10)

TABLE II: The fit parameters for the magnetic dipole form factor obtained for both a dipole and an exponential fit form with fit parameters $(g_0,\ m_0)$ and $(\tilde{g}_0,\ \tilde{m}_0)$, respectively.

C. The electric quadrupole form factor–G_{E2}

The sub-dominant electromagnetic quadrupole form factors G_{E2} and G_{C2} are extracted from the optimized sources S_2^V and S_3^V. The relevant expressions for a static Δ final state are [28]:

$$S_2^V(\mathbf{q};\mu) = -3A\Bigg\{\big((p_2+p_3)\delta_{1,\mu}+(p_3+p_1)\delta_{2,\mu}+(p_1+p_2)\delta_{3,\mu}\big)\mathcal{G}_{E2}(Q^2) - 2\frac{p_\mu}{\mathbf{p}^2}\big(p_1p_2+p_1p_3+p_2p_3\big)\left[\mathcal{G}_{E2}(Q^2)+\frac{E_N-m_\Delta}{2m_\Delta}\mathcal{G}_{C2}(Q^2)\right]\Bigg\}, \tag{21}$$

for the spatial current directions $\mu = 1,2,3$. For the temporal current direction $\mu = 4$, we have

$$S_2^V(\mathbf{q};\mu=4) = \frac{-i\ 6\ B}{\mathbf{p}^2}(p_1p_2+p_1p_3+p_2p_3)\mathcal{G}_{C2}(Q^2)\ , \tag{22}$$

where B is given by $B = \frac{\mathbf{p}^2}{2m_\Delta}A$, and A is the constant provided in Eq. 20.

Notice that the above combination, if used alone, will not allow for the extraction of G_{C2} at the lowest photon momentum $\mathbf{q} = (1,0,0)\frac{2\pi}{aL}$. Since chiral effects are stronger at low Q^2 values and experiments are targeted in that regime, we utilize the optimal linear three-function combination S_3^V in order to obtain G_{C2} also at the lowest Q^2 point allowed on the lattice. The corresponding expressions are

$$S_3^V(\mathbf{q};\mu) = -\frac{3\ A}{2}\ p_\mu\left[3\left(\delta_{\mu,3}-\frac{p_3^2}{\mathbf{p}^2}\right)\mathcal{G}_{E2}(Q^2)+\frac{E_N-m_\Delta}{2m_\Delta}\left(1-3\ \frac{p_3^2}{\mathbf{p}^2}\right)\mathcal{G}_{C2}(Q^2)\right] \tag{23}$$

for $\mu = 1,2,3$ and for the temporal component

$$S_3^V(\mathbf{q};\mu=4) = \frac{3\ i\ B}{2}\left(1-3\ \frac{p_3^2}{\mathbf{p}^2}\right)\mathcal{G}_{C2}(Q^2), \tag{24}$$

which is directly proportional to $G_{C2}(Q^2)$. Data obtained from both S_2^V and S_3^V are simultaneously fitted in the overconstrained analysis in order to extract the momentum dependence of G_{E2} and G_{C2} as accurately as possible.

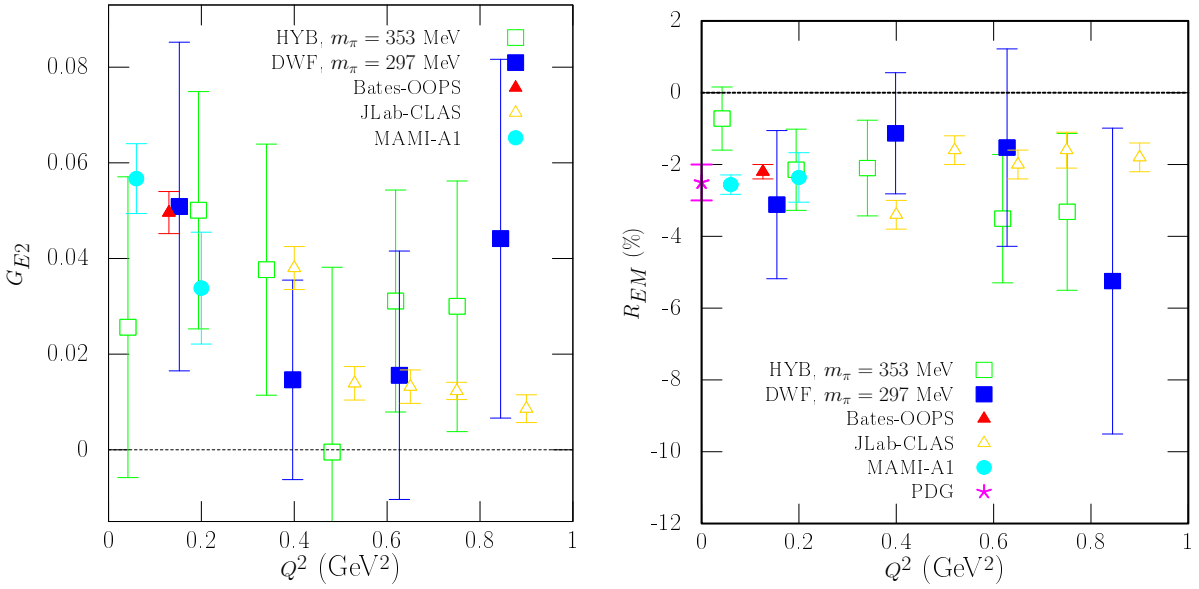

FIG. 4: In (a) the result of the electric quadrupole form factor $G_{E2}(Q^2)$ extracted from the fine DWF lattice measurements is shown. The results obtained from the hybrid action [28], as well as the experimentally extracted results from Bates [38–40], Jlab [41] and MAMI [42, 43] are also plotted for comparison. In (b) the corresponding R_{EM} evaluated in the rest frame of the Δ baryon ($\mathbf{p}' = 0$) is depicted for the fine DWF lattice as well as for the hybrid action [28]. The experimentally available results from [38–43] are also shown.

In Fig. 4(a) we plot the values of the electric quadrupole form factor G_{E2} for a range of values of $Q^2 < 1$ GeV^2, in the case of the fine DWF lattice. These results are compared to the results obtained from the mixed action [28]. We also mention here that in the case of the coarse DWF lattice the statistical noise on the G_{E2} and G_{C2} values is large, so a zero value can therefore not be excluded. The phenomenologically interesting ratio R_{EM} is defined as

$$R_{EM} = -\frac{G_{E2}(Q^2)}{G_{M1}(Q^2)}, \tag{25}$$

and has been used traditionally as a signal of deviation from spherical symmetry in the nucleon-Δ system. Early quark models as well as models of the proton wave function based on relativistic quarks including two-body exchange currents agree that a small R_{EM} value in the $-1 \sim 2\%$ regime should appear. The experimental values included in Fig. 4(a) show practically no dependence on Q^2. The same is true for the lattice data and in fact a good consistency with the experiment is

evident. The approach to the physical point can be predicted in chiral effective theory [33] where a non-monotonic dependence on the pion mass is expected with a minimum at 200 MeV. It is a significant challenge for the lattice to provide accurate results in the future in this regime in order to crosscheck the pion dynamics.

D. The Coulomb quadrupole form factor–G_{C2}

As mentioned in the previous section, the Coulomb quadrupole form factor is computed with the help of Eqs. (21)-(24). In the case of G_{C2}, Fig. 5(a) shows the results from the fine DWF lattice for values of $Q^2 < 1.5$ GeV^2. The values of $G_{C2}(Q^2)$ are positive and consistent with previous results obtained using the mixed action [28], and are also shown on the same figure. The experimentally measured ratio of Coulomb quadrupole to magnetic dipole form factor known also as CMR is defined by

$$R_{SM} = -\frac{|\mathbf{q}|}{2m_\Delta}\frac{G_{C2}(Q^2)}{G_{M1}(Q^2)}, \tag{26}$$

in the frame where the Δ is produced at rest. Lattice results on the R_{SM} ratio are shown in Fig. 5(b) where m_Δ in Eq. (26) is set to the physical mass. Known values of R_{SM} from various experiments are included in Fig. 5(b) and as with R_{EM} show almost no dependence on the momentum transfer. This is also the feature shown by the two lattice ensembles, the fine DWF at 297 MeV and the hybrid scheme at 353 MeV which are in very good agreement with each other. Despite the large statistical errors which escort the lattice values, they disagree with the experiment. Chiral effective theory predicts a monotonic decrease of this ratio as the pion mass approaches the chiral limit, which is different from the dependence of R_{EM}. The onset of large pion effects are expected below 300 MeV pions.

The overall conclusion is that QCD confirms non-zero quadrupole amplitudes pointing to the existence of the deformation in the $N-\Delta$ system, as coded in the EMR and CMR ratios. However, quantitative agreement with experiment has to await simulations at lighter pions masses, expected to become available in the next couple of years. Statistical accuracy at these light pions masses in particular for the sub-dominant form factors is an issue that has to be addressed. The use of the coherent source technique as employed here is a way to increase statistical accuracy.

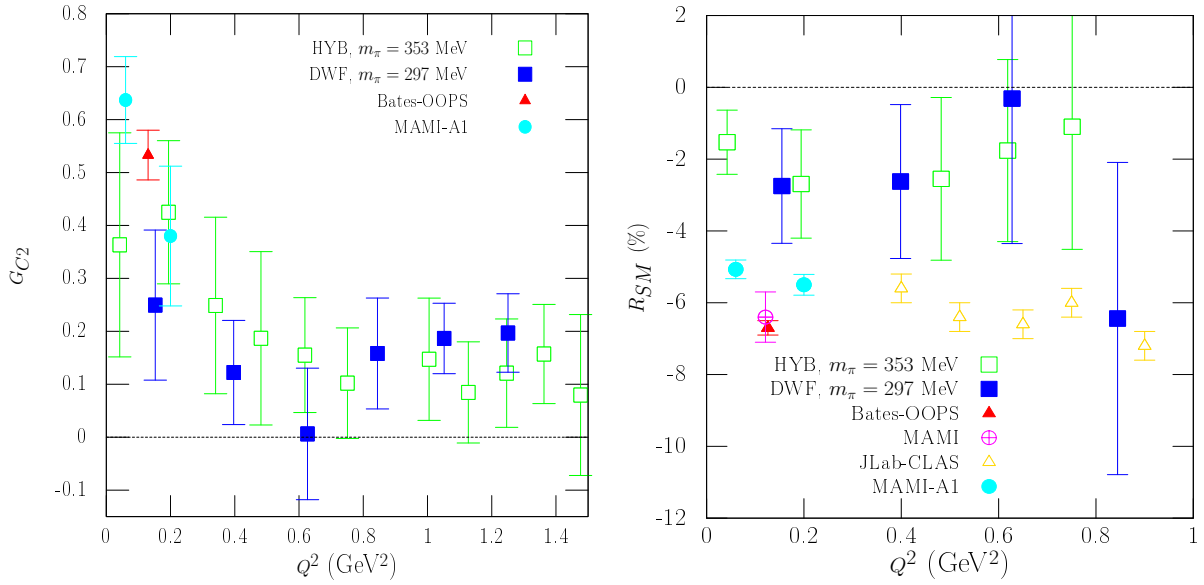

(a) (b)

FIG. 5: In plot (a) we show the Coulomb quadrupole form factor $G_{C2}(Q^2)$ extracted from the fine DWF lattice measurements. Along with it we provide also the result from the hybrid action approach [28]. Plot (b) depicts the corresponding R_{SM} evaluated in the rest frame of the Δ baryon. Non-zero values are confirmed, for the lowest Q^2 values accessible on the lattices. We also show results using the hybrid action taken from Ref. [28]. Experimental results are also included using the same notation as those in Fig. 4.

IV. AXIAL N TO Δ TRANSITION FORM FACTORS AND THE GOLDBERGER-TREIMAN RELATION

A. The Electro-weak and Pseudo-scalar transition matrix element

The nucleon to Δ matrix element of the axial vector current is parameterized in terms of four dimensionless form factors. In the Adler parameterization [44] it is written as follows

$$\langle \Delta(p',s')|A^3_\mu|N(p,s)\rangle \;=\; i\sqrt{\frac{2}{3}}\left(\frac{m_\Delta m_N}{E_\Delta(\mathbf{p}')E_N(\mathbf{p})}\right)^{1/2}\bar{u}^\lambda_{\Delta^+}(p',s')$$
$$\left[\left(\frac{C_3^A(q^2)}{m_N}\gamma^\nu + \frac{C_4^A(q^2)}{m_N^2}p'^\nu\right)\left(g_{\lambda\mu}g_{\rho\nu} - g_{\lambda\rho}g_{\mu\nu}\right)q^\rho + C_5^A(q^2)g_{\lambda\mu} + \frac{C_6^A(q^2)}{m_N^2}q_\lambda q_\mu\right]u_P(p,s) \qquad (27)$$

with the axial current given in Eq. (6).

The form factors $C_3^A(q^2)$ and $C_4^A(q^2)$ belong to the transverse part of the axial current and are both suppressed [27] relative to the longitudinal form factors $C_5^A(q^2)$ and $C_6^A(q^2)$, which are the dominant ones and are the ones considered in this work.

Likewise, the pseudo-scalar transition form factor $G_{\pi N\Delta}(q^2)$, is defined via

$$2m_q\langle\Delta(p',s')|P^3|N(p,s)\rangle = i\sqrt{\frac{2}{3}}\left(\frac{m_\Delta m_N}{E_\Delta(\mathbf{p}')E_N(\mathbf{p})}\right)^{1/2}\frac{f_\pi m_\pi^2\, G_{\pi N\Delta}(q^2)}{m_\pi^2-q^2}\bar{u}^\nu_{\Delta^+}(p',s')\frac{q_\nu}{2m_N}u_P(p,s) \tag{28}$$

where the normalization of the RHS of (28) is chosen such that $G_{\pi N\Delta}(q^2)$ reproduces the phenomenological coupling of the $\pi - N - \Delta$ vertex in the strong interaction Lagrangian,

$$\mathcal{L}_{\pi N\Delta} = \frac{g_{\pi N\Delta}}{2m_N}\bar{\Delta}_\mu\partial_\mu\vec{\pi}\cdot\vec{\tau}\;N + \text{h.c.} \tag{29}$$

and the pseudo-scalar density is defined in Eq. (6). In the SU(2) symmetric limit with m_q denoting the up/down mass, the pseudo-scalar density is related to the divergence of the axial-vector current through the axial Ward-Takahashi identity (AWI)

$$\partial^\mu A^a_\mu = 2m_q P^a\ . \tag{30}$$

Taking matrix elements of the above identity between N and Δ states leads to the non-diagonal Goldberger-Treiman (GT) relation

$$C_5^A(q^2) + \frac{q^2}{m_N^2}C_6^A(q^2) = \frac{1}{2m_N}\frac{G_{\pi N\Delta}(q^2)f_\pi m_\pi^2}{m_\pi^2-q^2}\quad . \tag{31}$$

On the other hand, flavor symmetry in the hadronic world is expressed through the partially-conserved axial vector current (PCAC) hypothesis

$$\partial^\mu A^a_\mu = f_\pi m_\pi^2\pi^a \tag{32}$$

which relates the pseudo-scalar current to the pion field operator and the pion decay constant f_π which is here is taken to be 92 MeV. From Eqs. (30) and (32) the pion field π^a is related to the pseudo-scalar density via

$$\pi^a = \frac{2m_q P^a}{f_\pi m_\pi^2}. \tag{33}$$

Assuming pion pole dominance we can relate the form factor C_6^A to $G_{\pi N\Delta}$ through:

$$\frac{1}{m_N}C_6^A(q^2)\ \sim\ \frac{1}{2}\frac{G_{\pi N\Delta}(q^2)f_\pi}{m_\pi^2-q^2} \tag{34}$$

Then, substituting Eq. (34) in Eq. (31), we obtain the simplified Goldberger-Treiman (GT) relation

$$G_{\pi N\Delta}(q^2)\,f_\pi\ =\ 2m_N C_5^A(q^2) \tag{35}$$

in an analogous fashion to the well known GT relation which holds in the nucleon sector studied on the lattice in Ref. [21]. Pion pole dominance therefore fixes completely the ratio $C_6^A(q^2)/C_5^A(q^2)$ as a pure monopole term

$$\frac{C_6^A(q^2)}{C_5^A(q^2)} = \frac{m_N^2}{m_\pi^2 - q^2} \quad . \tag{36}$$

The aim here is to calculate the dominant axial $C_5^A(q^2)$, $C_6^A(Q^2)$, as well as the pseudo-scalar $G_{\pi N\Delta}(Q^2)$ form factor and examine the validity of the GT relations within the dynamical DWF framework, using both the coarse and fine DWF lattices.

B. The dominant axial C_5^A, C_6^A transition form factors

The extraction of the axial transition form factors requires data from two sets of the optimal Δ sinks, namely S_1 and S_2, which are introduced in section II, for the local isovector axial-vector current insertion $A_\mu^3(x)$. The corresponding expressions for the large Euclidean time separation ratios are:

$$\begin{aligned} S_1^A(\mathbf{q};j) =& B\Bigg[-\frac{C_3^A}{2}\Bigg\{ (E_N - 2m_\Delta + m_N) + \left(\sum_{k=1}^{3} p^k\right) \frac{p^j}{E_N + m_N} \Bigg\} \\ & - \frac{m_\Delta}{m_N}(E_N - m_\Delta) C_4^A + m_N C_5^A - \frac{C_6^A}{m_N} p^j \left(\sum_{k=1}^{3} p^k\right) \Bigg], \end{aligned} \tag{37}$$

for spatial components $j = 1, 2, 3$ of the axial current, and

$$S_1^A(\mathbf{q};4) = -iB \sum_{k=1}^{3} p^k \left[C_3^A + \frac{m_\Delta}{m_N} C_4^A + \frac{E_N - m_\Delta}{m_N} C_6^A \right], \tag{38}$$

for the temporal component. Since the four form factors are not completely decoupled by the above relations, we also employ the optimal Δ sink S_2^A given in the plateau by

$$S_2^A(\mathbf{q};j) = i\frac{3A}{2}\left[\left(\sum_{k=1}^{3} p^k\right) \left(\delta_{j,1}(p^2 - p^3) + \delta_{j,2}(p^3 - p^1) + \delta_{j,3}(p^1 - p^2)\right) C_3^A \right], \tag{39}$$

valid for spatial components $j = 1, 2, 3$. The kinematical factors A and B are given by

$$A = \frac{B}{(E_N + m_N)} \quad , \quad B = \sqrt{\frac{2}{3}} \frac{\sqrt{(E_N + m_N)/E_N}}{3m_N} \, . \tag{40}$$

Data from S_1^A and S_2^A determine all four form factors C_3^A, C_4^A, C_5^A and C_6^A at each value of Q^2 in a simultaneous overconstrained analysis. Z_A is required to renormalize the axial vector operator. This has been computed by the UKQCD-RBC and LHP collaborations for both ensembles [11, 31,

34]. The values provided in Table I confirm that $Z_V = Z_A + O(a^2)$ in the chiral limit, as expected for the manifestly chiral DWF action.

The results for the axial dominant form factor C_5^A from the two DWF lattices considered in this work are presented in Fig. 6(a) and are in good agreement with the results obtained from the mixed action approach at $m_\pi = 353$ MeV [21]. The Q^2 dependence is well described by two-parameter dipole (solid line) and exponential (dashed line) forms $d_0/(1+Q^2/m_A^2)^2$, $\tilde{d}_0 \exp(-Q^2/\tilde{m}_A^2)$, respectively, which are almost indistinguishable in the plot. The fitted values for $C_5^A(0) \equiv d_0$ (or $\tilde{d}_0$ of the exponential form) and the corresponding axial mass $m_A\,(\tilde{m}_A)$ are given in Table III. In the same figure, we also show a dipole fit to the available experimental data [45] which determine an axial mass within the range of values of $m_A \sim 0.85 - 1.1$ GeV [45, 46], obtained from the pure dipole parameterization. As in the case of $G_{M1}(Q^2)$, we observe a flatter slope for the lattice data, reflected in the larger value of the axial mass m_A extracted from the lattice results.

m_π [GeV]	m_A [GeV]	d_0	$\tilde{m}_A$ [GeV]	$\tilde{d}_0$	m [GeV]	c_0	Δ'	$g_{\pi N\Delta}$	
coarse $N_F = 2+1$ DWF								(K)	(α')
0.329(1)	1.588(70)	0.970(30)	1.262(36)	0.940(21)	0.509(15)	5.132(204)	0.030(5)	9.525(168)	13.936(588)
fine $N_F = 2+1$ DWF									
0.297(5)	1.699(170)	0.944(58)	1.314(98)	0.927(46)	0.507(33)	5.756(516)	0.037(6)	8.444(491)	16.257(867)
Hybrid action									
0.353(3)	1.795(40)	0.903(11)	1.386(18)	0.888(8)	0.496(10)	5.613(150)	0.019(11)	9.323(219)	11.446(617)

TABLE III: The first column gives the pion mass in GeV. The second and third columns provide the dipole fit parameters m_A and d_0 extracted from fitting C_5^A to $d_0/(1+Q^2/m_A^2)^2$, the fourth and fifth columns the corresponding parameters obtained from the use of an exponential ansatz $\tilde{d}_0 \exp(-Q^2/\tilde{m}_A^2)$, the sixth and seventh columns the fit parameters m and c_0 extracted from fitting the ratio C_6^A/C_5^A to a monopole form $c_0/(1+Q^2/m^2)$ for the N–to–Δ process. The eighth and ninth columns show the calculated values of the fit parameters α' and Δ' defined in the linear fit of Eq. (51). The last two columns give the predicted values of the strong coupling constant $g_{\pi N\Delta} \equiv G_{\pi N\Delta}(0)$. The first value of the strong coupling constant is determined using the fit function of Eq. (50), while the second uses the linear fit based on Eq. (51), which is exactly equal to α'.

In Fig. 6(b) we show the ratio C_6^A/C_5^A, since ratios of this type are expected to be less prone to lattice artifacts. The dashed black line shows the pion pole dominance prediction of Eq. (36), where for m_N and m_π we use the lattice extracted values that correspond to the fine DWF lattice. The predicted curve does not describe the data at low-Q^2 i.e., in the regime where the strong pion cloud effects are expected to be present. However, the fit to the monopole form $c_0/(1+Q^2/m^2)$

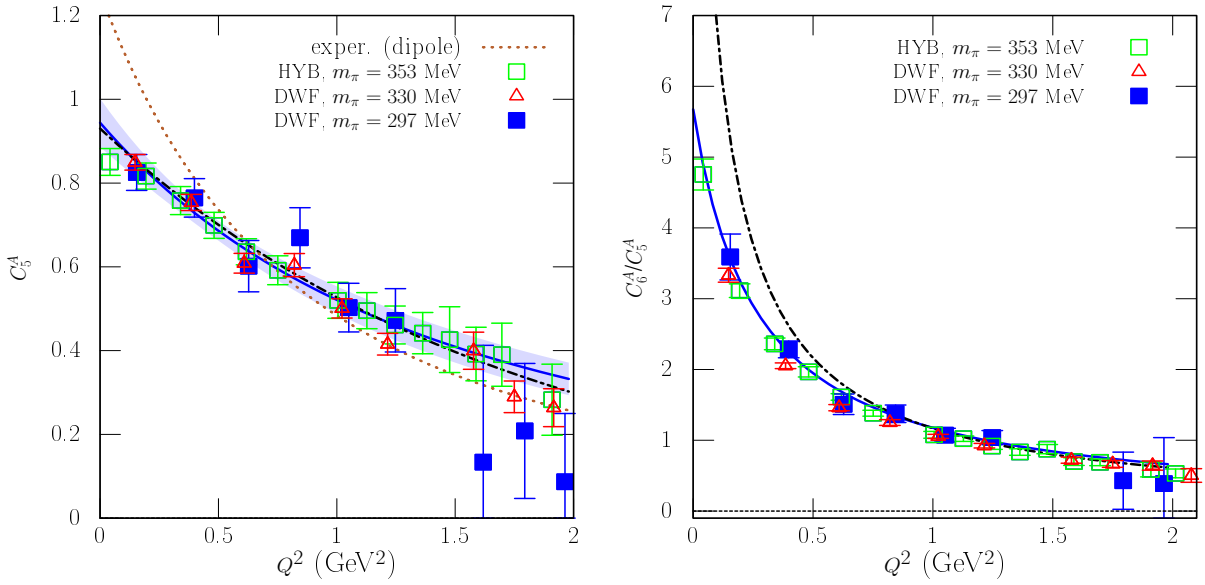

(a) (b)

FIG. 6: Plot (a) shows the Q^2-dependence of the axial form factor C_5^A extracted from the coarse and fine DWF lattices. The corresponding mixed action results [21] have also been included. The solid blue (dashed black) line is from the dipole (exponential) fit for to the fine DWF lattice results. Note that the error band corresponds to the dipole fit. The dotted brown line is the dipole fit to the experimental data. The ratio C_6^A/C_5^A versus Q^2 is plotted in (b). The dashed black line refers to the fine DWF lattice results and is the pion pole dominance prediction of Eq. (36). The solid blue line is a fit to a monopole form $c_0/(1+Q^2/m^2)$.

describes satisfactorily the ratio yielding a heavier mass parameter m than the lattice value of the pion mass (see Table III). Such behavior has been observed also for the hybrid and quenched Wilson actions [21].

The lattice results for the C_6^A are plotted on Fig. 7. The curve shown (solid line) in the figure corresponds to the form

$$\frac{d_0\ c_0}{(1+Q^2/m_A^2)^2(1+Q^2/m^2)}, \tag{41}$$

where c_0 and m are the parameters of the monopole term given in Eq. (36) that are expected to describe well the C_6^A/C_5^A ratio provided the pion pole dominance is applicable. The form described by the expression of Eq. (41), seems to provide the best fit to the fine DWF data. On the other hand, C_6^A is related to the C_5^A form factor through the expression

$$C_6^A(Q^2) = C_5^A(Q^2)\ \frac{m_N^2}{m_\pi^2+Q^2}.$$

The curve that corresponds to the dashed line is obtained from fitting the fine DWF data to this

form. In this case C_5^A is being described by the dipole form shown in Fig. 6(a), while the nucleon and pion masses are the lattice evaluated ones.

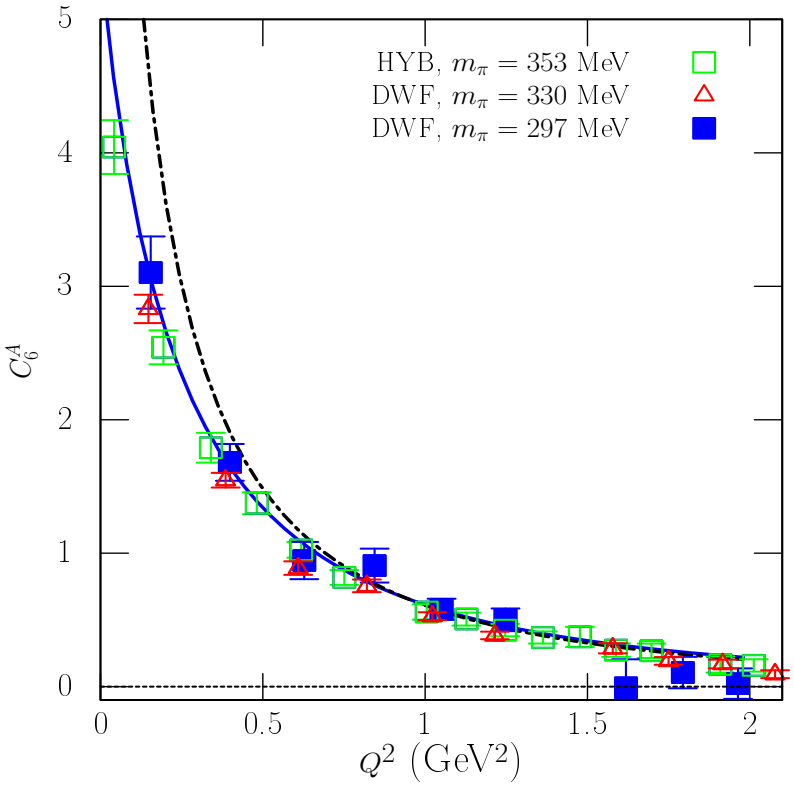

FIG. 7: Lattice results for C_6^A are shown as a function of Q^2. The solid blue line is the fit to the form of Eq. (41), while the dashed black line corresponds to the form $C_5^A\left(\frac{m_N^2}{m_\pi^2+Q^2}\right)$. Note that for the latter fit, the C_5^A factor is described by the dipole fit parameters.

C. The Pseudo-scalar transition form factor and Goldberger-Treiman relation

The pseudo-scalar form factor $G_{\pi N\Delta}(Q^2)$, defined via the matrix element given in Eq. (28), is extracted directly from the optimized linear combination S_1 with the pseudo-scalar current operator insertion of Eq. (6). In the large Euclidean time limit where only the nucleon and Δ states dominate the corresponding ratio yields

$$S_1^P(\mathbf{q}\,;\,\gamma_5) = \sqrt{\frac{2}{3}}\sqrt{\frac{E_N+m_N}{E_N}}\left[\frac{q_1+q_2+q_3}{6m_N}\frac{f_\pi m_\pi^2}{2m_q(m_\pi^2+Q^2)}\right] G_{\pi N\Delta}(Q^2) \quad . \tag{42}$$

Notice that the extraction of $G_{\pi N\Delta}$ from the above equation requires knowledge of the quark mass m_q and the pion decay constant, f_π, on the given ensembles. Calculation of f_π requires the

two-point functions of the axial-vector current A_4^3 with local-smeared (LS) and smeared-smeared (SS) quark sources,

$$C_{LS}^A(t) = \sum_{\mathbf{x}} \langle \Omega |\ T\ \left(A_4^3(\mathbf{x},t) \tilde{A}_4^3(\mathbf{0},0) \right)\ | \Omega \rangle \tag{43}$$

(and similarly for C_{SS}^A), where $A_4^3(\mathbf{x},t)$ denotes the local operator and $\tilde{A}_4^3(\mathbf{x},t)$ the smeared operator. The pion-to-vacuum matrix element

$$\langle 0 | A_\mu^a(0) | \pi^b(p) \rangle = i f_\pi p_\mu \delta^{ab} \tag{44}$$

is extracted from the two-point functions C_{LS}^A and C_{SS}^A and

$$f_\pi^{\rm eff}(t) = Z_A \sqrt{\frac{2}{m_\pi}} \frac{C_{LS}^A(t)}{\sqrt{C_{SS}^A(t)}}\ e^{m_\pi t/2} \quad . \tag{45}$$

yields f_π in the large Euclidean time limit.

The renormalized quark mass m_q is determined from the AWI, via two-point functions of the pseudoscalar density with either local (P^3) or smeared ($\tilde{P}^3$) quark fields,

$$C_{LS}^P(t) = \sum_{\mathbf{x}} \langle \Omega |\ T\ \left(P^3(\mathbf{x},t) \tilde{P}^3(\mathbf{0},0) \right)\ | \Omega \rangle\ , \tag{46}$$

(and similarly for C_{SS}^P). The effective quark mass is defined by

$$m_{\rm eff}^{\rm AWI}(t) = \frac{m_\pi}{2} \frac{Z_A}{Z_P} \frac{C_{LS}^A(t)}{C_{LS}^P(t)} \sqrt{\frac{C_{SS}^P(t)}{C_{SS}^A(t)}}\ . \tag{47}$$

and its plateau value yields m_q. Note that Z_P will be needed only if ones wants m_q alone. Since Z_P enters also Eq. (42) it cancels –as does Z_A since it comes with f_π– and therefore $G_{\pi N\Delta}$ is extracted directly from ratios of lattice three- and two-point functions without prior knowledge of either Z_A or Z_P. We also note that the quark mass computed through (47) includes the effects of residual chiral symmetry breaking from the finite extent L_5 of the fifth dimension. These effects are of the order of 60% for the coarse ensemble and 17% for the fine ensemble. Chiral symmetry breaking affects the PCAC relations and therefore the value of $G_{\pi N\Delta}$ through Eq. (42).

The ratio

$$\frac{f_\pi G_{\pi N\Delta}(Q^2)}{2 m_N C_5^A(Q^2)} \tag{48}$$

is depicted in Fig. 8(a). It should be *unity* if the off-diagonal Goldberger-Treiman relation of Eq. (35) is satisfied, which in turn requires that PCAC holds exactly at the pion masses simulated in these ensembles. Deviations from this relation are seen in the low-Q^2 regime. For the fine ensemble

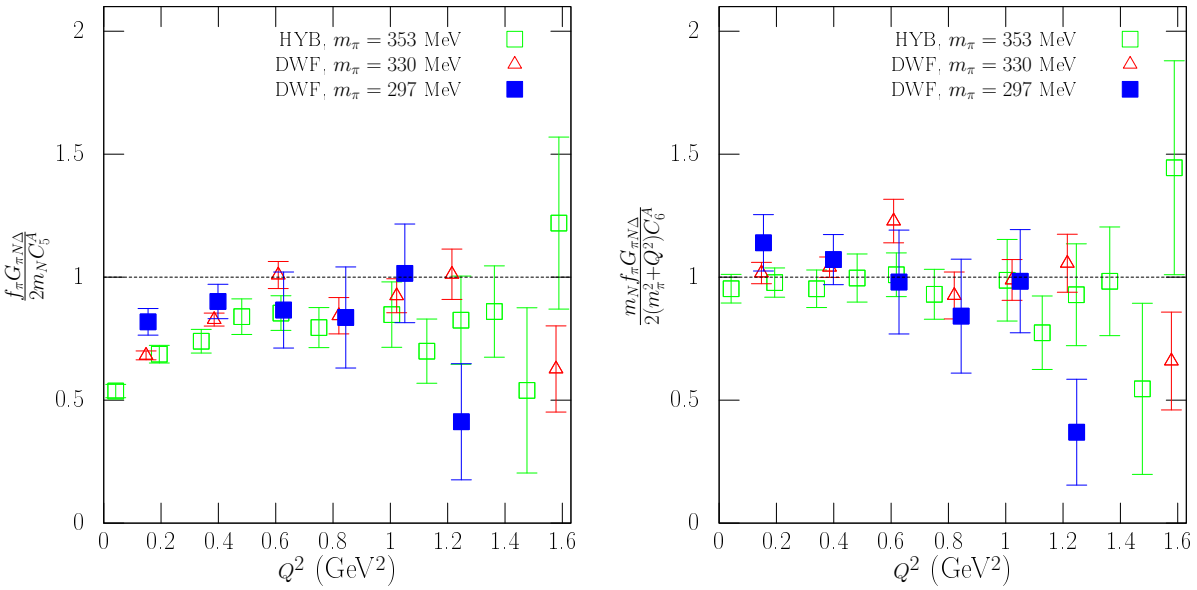

FIG. 8: In (a) we plot the ratio of Eq. (48) as a function of Q^2 as a validity test of the GT relation. Similarly, in plot (b) ratio of Eq. (49) that relates to the validity of Eq. (34).

considered in this study, the deviations from unity are less severe. At momentum transfers, of about $Q^2 \gtrsim 0.5$ GeV^2, the relation is at least approximately satisfied and it is consistent among all actions considered here.

Pion pole dominance relates C_6^A to C_5^A through Eq. (36), which is very well satisfied by the lattice data for all the actions employed in this work (see also Fig. 6(b)). This agreement is also evident from Fig. 8(b), where the ratio

$$\frac{m_N f_\pi G_{\pi N\Delta}(Q^2)}{2(m_\pi^2+Q^2)C_6^A(Q^2)} \tag{49}$$

is consistent with unity.

In Fig. 9 we compare results on $G_{\pi N\Delta}(q^2)$ using the dynamical DWF lattices to the results obtained from the hybrid scheme taken from Ref. [21]. There is an agreement for $Q^2 > 0.5$ GeV^2 whereas for lower Q^2 values the fine DWF data appear to be higher than the data from the other two lattices. The solid line is a one-parameter fit form to the fine DWF data

$$G_{\pi N\Delta}(Q^2) = K\,\frac{(Q^2/m_\pi^2+1)}{(Q^2/m_A^2+1)^2(Q^2/m^2+1)}, \tag{50}$$

which is expected assuming the validity of Eq. (36). The fit parameter K provides an estimate of

the strong coupling $g_{\pi N\Delta}$ at $Q^2 = 0$. In addition, we fit to the ansatz

$$G_{\pi N\Delta}(Q^2) = \alpha' \left(1 - \Delta' \frac{Q^2}{m_\pi^2}\right), \tag{51}$$

shown by the dashed line. The fit parameters are provided in Table III. As can be seen, despite the fact that both fits describe sufficiently well the data for $0.5 \lesssim Q^2 \lesssim 1.5$ GeV^2, they yield quite different values at $Q^2 = 0$ prohibiting a reliable evaluation of $g_{\pi N\Delta}$. Clearly, in order to achieve this goal, a better understanding of the behavior at low-Q^2 is required, since this quantity is sensitive to pion loop effects that maybe affected by lattice artifacts such as the finite-L_5 extent.

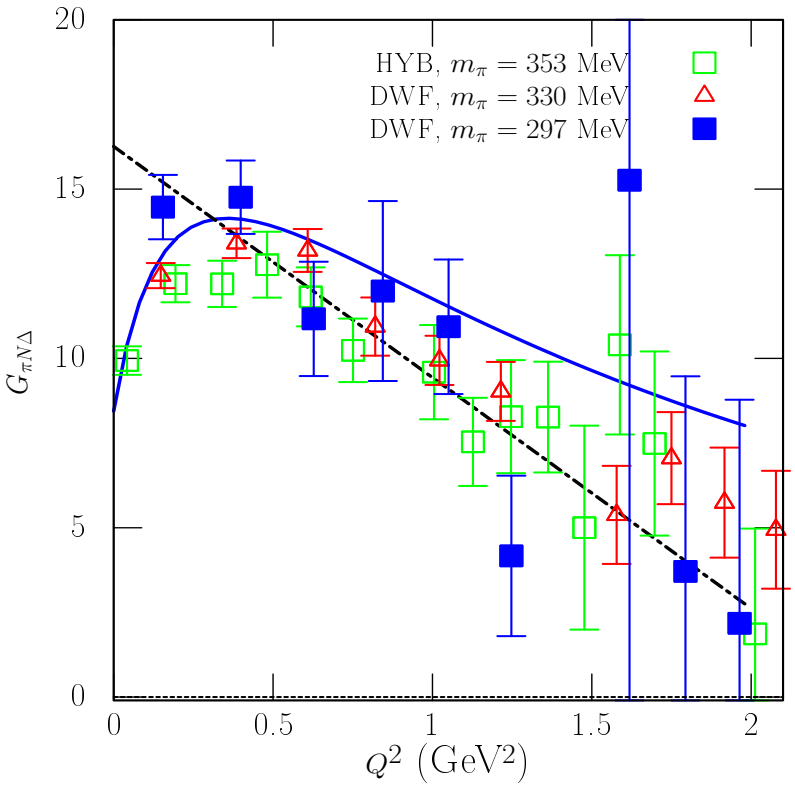

FIG. 9: The plot shows the Q^2-dependence of the pseudo-scalar transition form factor $G_{\pi N\Delta}$. The solid blue line is a fit to pion pole dominance form of Eq. (50) for the fine DWF ensemble. The dashed black line is the linear fit given by Eq. (51). The strong coupling constant $g_{\pi N\Delta}$ is the value of $G_{\pi N\Delta}$ at $Q^2 = 0$.

Finally, from our lattice results we can predict the currently unmeasured ratio C_5^A/C_3^V, which is an important first approximation to the parity violating asymmetry. Its dependence in Q^2 is depicted in Fig. 10. From the plot we can see a very good agreement between the coarse and fine DWF data, at least in the range up to $Q^2 \sim 1.0$ GeV, indicating that there are no lattice cut-off effects regarding this quantity. It is also evident from the plot that at $Q^2 = 0$ the ratio is expected

to have a non-zero value. It is noted that C_3^V is computed from the relationship

$$C_3^V = \frac{3}{2}\,\frac{m_\Delta(m_N+m_\Delta)}{2(m_N+m_\Delta)^2+Q^2}\,(G_{M1}-G_{E2}) \tag{52}$$

and is therefore dominated by G_{M1}. As both C_5^A and G_{M1} lack chiral effects near the origin, the ratio C_5^A/C_3^V is expected to be less sensitive to such effects. The present results for C_5^A/C_3^V are

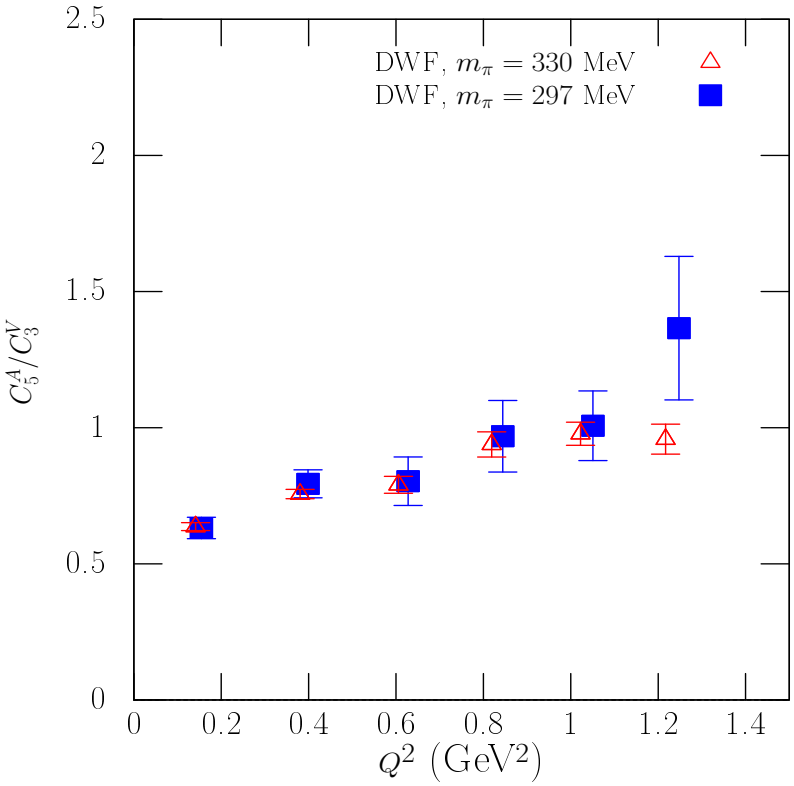

FIG. 10: The plot describes the Q^2-dependence of the ratio C_5^A/C_3^V. The results shown are those extracted from both DWF lattices considered in this work.

also consistent within statistics with the results reported earlier in Ref. [27].

V. CONCLUSIONS

The nucleon to Δ electromagnetic, axial and pseudoscalar transition form factors are calculated using $N_f = 2+1$ dynamical domain wall fermions for pion masses of 330 MeV and 297 MeV for Q^2 values up to about 2 GeV^2. There is qualitative agreement between results obtained in the unitary theory and corresponding results obtained using valence domain wall quarks on a staggered sea. The momentum dependence of the dominant magnetic dipole, G_{M1}, and axial, C_5^A, form factors are well described by dipole forms. They both show a slower fall-off with Q^2 than the comparison

to the experimental data, a fact that is reflected in the heavier dipole masses that fit the lattice data. Pion cloud effects are expected to dominate the low-Q^2 dependence and therefore simulations with pion mass below 300 MeV are required in order to allow the evaluation of such effects from first principles.

The phenomenologically interesting sub-dominant electromagnetic quadrupole form factors G_{E2} and G_{C2} have been calculated in the case of the fine DWF lattice using the coherent sink technique in order to increase the statistical accuracy. The results confirm a non-zero value at low $Q^2 \leq 1$ GeV^2. The EMR and CMR ratios are almost Q^2 independent. The EMR values are in agreement with the experiment, whereas the strength of the CMR is underestimated. This can be understood in chiral effective theory, which predicts different chiral behavior for the two quantities. The non-zero values calculated in QCD are in accord with the experimental determinations [8, 38, 40–43] and confirm a deviation from spherical symmetry in the Nucleon-Δ system.

The axial transition form factor C_6^A is dominated by chiral symmetry breaking dynamics, which is directly reflected in the pion pole dominance. In addition, the pseudoscalar form factor $G_{\pi N\Delta}$ is computed and the non-diagonal Goldberger-Treiman relation, which is a direct consequence of PCAC is shown to be well satisfied by the lattice data, especially for the lowest mass on the fine DWF ensemble. Pure monopole dependence of the C_6^A/C_5^A ratio is well satisfied, but with monopole masses considerably heavier than the corresponding lattice pion masses. The low-Q^2 dependence of $G_{\pi N\Delta}$ appears to be non-trivial and the extraction of the phenomenological strong $\pi - N - \Delta$ coupling, $g_{\pi N\Delta}$, requires careful understanding of the matrix element systematics, since it will be sensitive to both chiral and lattice cutoff effects.

In conclusion, the $N - \Delta$ transition yields valuable information that is complementary to nucleon and Delta form factors. Also, since the transition is isovector, it provides an opportunity to assess the importance of disconnected quark loop effects. Furthermore, it provides constraints on the low energy constants that enter the chiral effective description of hadron properties. This work, utilizing dynamical chiral fermions corresponding to pion masses of 297 MeV and 330 MeV, together with related calculations of nucleon and Delta form factors, is a significant advance in the quest to understand from first principles how the closely related structure of the nucleon and Delta arise from QCD. The outstanding challenge for the future is to extend these calculations to the physical pion mass and reduce statistical and systematic errors to the level of a few percent. It is an appealing challenge for Lattice QCD to perform precise calculations for pion masses that approach the physical point with all systematics under control. Simulations with pions almost at its physical value will soon become available and it will be important to continue the investigation

of these quantities.

Acknowledgments

This research was partly supported by the Cyprus Research Promotion Foundation (R.P.F) under contracts No. ΠΕΝΕΚ/ΕΝΙΣΧ/0505-39 and No. EPYAN/0506/08 and by the U.S. Department of Energy under Grant No. DE-FG02-94ER-40818. The authors would also like to acknowledge the use of dynamical domain wall fermions configurations provided by the RBC-UKQCD collaborations, the forward propagators provided by the LHPC and the use of Chroma software [47].

---

[1] H.-Y. Gao, Int. J. Mod. Phys. **E12**, 1 (2003), nucl-ex/0301002.

[2] C. E. Hyde-Wright and K. de Jager, Ann. Rev. Nucl. Part. Sci. **54**, 217 (2004).

[3] C. F. Perdrisat, V. Punjabi, and M. Vanderhaeghen, Prog. Part. Nucl. Phys. **59**, 694 (2007), hep-ph/0612014.

[4] J. Arrington, C. D. Roberts, and J. M. Zanotti, J. Phys. **G34**, S23 (2007), nucl-th/0611050.

[5] A. V. Afanasev, S. J. Brodsky, C. E. Carlson, Y.-C. Chen, and M. Vanderhaeghen, Phys. Rev. **D72**, 013008 (2005), hep-ph/0502013.

[6] C. N. Papanicolas, (ed.) and A. M. Bernstein, (ed.), AIP Conference Proceedings **904**, 1 (2007), prepared for Workshop on the Shape of Hadrons, Athens, Greece, 27-29 Apr 2006.

[7] A. M. Bernstein and C. N. Papanicolas, AIP Conf. Proc. **904**, 1 (2007), 0708.0008.

[8] C. N. Papanicolas, Eur. Phys. J. **A18**, 141 (2003).

[9] C. Alexandrou, PoS **LAT2010** (2010).

[10] T. Yamazaki et al., Phys. Rev. **D79**, 114505 (2009), 0904.2039.

[11] S. N. Syritsyn et al., Phys. Rev. **D81**, 034507 (2010), 0907.4194.

[12] J. D. Bratt et al. (LHPC) (2010), 1001.3620.

[13] C. Alexandrou et al., PoS **LAT2009**, 145 (2009), 0910.3309.

[14] C. Alexandrou, G. Koutsou, J. W. Negele, and A. Tsapalis, Phys. Rev. **D74**, 034508 (2006), hep-lat/0605017.

[15] S. Ohta and T. Yamazaki (for RBC and UKQCD) (2008), 0810.0045.

[16] T. Gorringe and H. W. Fearing, Rev. Mod. Phys. **76**, 31 (2004), nucl-th/0206039.

[17] V. Bernard, L. Elouadrhiri, and U. G. Meissner, J. Phys. **G28**, R1 (2002), hep-ph/0107088.

[18] R. G. Edwards et al. (LHPC), Phys. Rev. Lett. **96**, 052001 (2006), hep-lat/0510062.

[19] A. A. Khan et al., Phys. Rev. **D74**, 094508 (2006), hep-lat/0603028.

[20] T. Yamazaki et al. (RBC+UKQCD), Phys. Rev. Lett. **100**, 171602 (2008), 0801.4016.

[21] C. Alexandrou, G. Koutsou, T. Leontiou, J. W. Negele, and A. Tsapalis, Phys. Rev. **D76**, 094511 (2007), 0706.3011.

[22] D. B. Leinweber, T. Draper, and R. M. Woloshyn, Phys. Rev. **D48**, 2230 (1993), hep-lat/9212016.

[23] C. Alexandrou et al., Phys. Rev. **D69**, 114506 (2004), hep-lat/0307018.

[24] C. Alexandrou, Nucl. Phys. Proc. Suppl. **128**, 1 (2004), nucl-th/0311007.

[25] C. Alexandrou et al., Phys. Rev. Lett. **94**, 021601 (2005), hep-lat/0409122.

[26] C. Alexandrou et al., Nucl. Phys. Proc. Suppl. **140**, 293 (2005), hep-lat/0408017.

[27] C. Alexandrou, T. Leontiou, J. W. Negele, and A. Tsapalis, Phys. Rev. Lett. **98**, 052003 (2007), hep-lat/0607030.

[28] C. Alexandrou et al., Phys. Rev. **D77**, 085012 (2008), 0710.4621.

[29] C. Alexandrou et al., PoS **LAT2005**, 091 (2006), hep-lat/0509140.

[30] C. Alexandrou, G. Koutsou, T. Leontiou, J. W. Negele, and A. Tsapalis, PoS **LAT2007**, 162 (2007), 0710.2173.

[31] C. Allton et al., Phys. Rev **D78**, 114509 (2008).

[32] C. Alexandrou et al. (2009), 0910.5617.

[33] V. Pascalutsa and M. Vanderhaeghen, Phys. Rev. Lett. **95**, 232001 (2005), hep-ph/0508060.

[34] Y. Aoki et al., Phys. Rev. **D 78**, 054510 (2008), 0910.3309.

[35] E. E. Scholz (RBC-UKQCD Collaborations), PoS **LATTICE2008**, 095 (2008).

[36] P. Hägler et al. (LHPC), Phys. Rev. **D68**, 034505 (2003), hep-lat/0304018.

[37] C. W. Bernard et al., Phys. Rev. **D64**, 054506 (2001), hep-lat/0104002.

[38] C. Mertz et al. (OOPS), Phys. Rev. Lett. **86**, 2963 (2001), nucl-ex/9902012.

[39] N. F. Sparveris et al. (OOPS), Phys. Rev. **C67**, 058201 (2003), nucl-ex/0212022.

[40] N. F. Sparveris et al. (OOPS), Phys. Rev. Lett. **94**, 022003 (2005), nucl-ex/0408003.

[41] K. Joo et al. (CLAS), Phys. Rev. Lett. **88**, 122001 (2002), hep-ex/0110007.

[42] S. Stave et al., Eur. Phys. J. **A30**, 471 (2006), nucl-ex/0604013.

[43] N. F. Sparveris et al., Phys. Lett. **B651**, 102 (2007), nucl-ex/0611033.

[44] J. C. Alder et al., Nucl. Phys. **B46**, 573 (1972).

[45] T. Kitagaki et al., Phys. Rev. **D42**, 1331 (1990).

[46] E. Hernández et al., Phys. Rev. **D81**, 085046 (2010).

[47] R. G. Edwards and B. Joo (SciDAC Collaboration, LHPC Collaboration and UKQCD Collaboration), Nucl. Phys. Proc. Suppl. **140**, 832 (2005), hep-lat/0409003.

VI. APPENDIX

Q^2 (GeV^2)	G_{M1}
DWF ($N_f = 2+1$), $a^{-1} = 1.73$ GeV, $m_\pi = 330$ MeV	
0.141	1.581(40)
0.380	1.198(32)
0.605	0.933(33)
0.819	0.786(39)
1.022	0.641(30)
1.217	0.545(33)
1.584	0.449(50)
1.757	0.369(42)
1.925	0.332(51)
2.088	0.238(48)
2.247	0.204(99)

TABLE IV: Coarse DWF results for G_{M1}, their Q^2-dependence and the corresponding (form factor) jackknife statistical errors.

Q^2 (GeV^2)	G_{M1}	G_{E2}	EMR (%)	G_{C2}	CMR (%)
DWF ($N_f = 2+1$), $a^{-1} = 2.34$ GeV, $m_\pi = 297$ MeV					
0.154	1.602(93)	0.0508(344)	-3.118(2.064)	0.249(142)	-2.748(1.595)
0.398	1.168(75)	0.0146(208)	-1.129(1.686)	0.122(98)	-2.624(2.144)
0.627	0.928(84)	0.0156(259)	-1.528(2.749)	0.006(124)	-3.145(4.036)
0.844	0.875(101)	0.0441(375)	-5.246(4.259)	0.158(105)	-6.439(4.348)
1.051	0.593(72)	0.0261(225)	4.263(3.707)	0.186(67)	-12.490(4.742)
1.248	0.417(86)	0.0206(251)	4.874(5.781)	0.197(74)	-20.847(8.769)
1.620	0.439(44)				
1.802	0.224(159)				
1.964	0.165(181)				

TABLE V: DWF results for G_{M1}, G_{E2}, EMR (%), G_{C2} and CMR (%) along with their Q^2-dependence shown in the first column. The errors shown are statistical jackknife errors.

Q^2 (GeV^2)	C_5^A	C_6^A	$G_{\pi N\Delta}$
DWF ($N_f = 2+1$), $a^{-1} = 1.73$ GeV, $m_\pi = 330$ MeV			
0.141	0.849(19)	2.831(106)	12.446(371)
0.380	0.754(19)	1.547(55)	13.379(436)
0.605	0.608(24)	0.888(51)	13.187(633)
0.819	0.604(27)	0.755(47)	10.941(86)
1.022	0.500(23)	0.528(29)	9.943(727)
1.217	0.415(26)	0.383(28)	9.026(870)
1.584	0.399(44)	0.287(38)	5.379(1.448)
1.757	0.289(38)	0.193(28)	5.741(1.625)
1.925	0.263(45)	0.169(33)	7.055(1.359)
2.247	0.186(46)	0.093(29)	4.942(1.740)
DWF ($N_f = 2+1$), $a^{-1} = 2.34$ GeV, $m_\pi = 297$ MeV			
0.154	0.825(42)	3.103(270)	15.292(1.005)
0.398	0.764(46)	1.680(138)	15.601(1.145)
0.627	0.601(61)	0.945(139)	11.803(1.784)
0.844	0.669(72)	0.907(127)	12.672(2.807)
1.051	0.502(158)	0.579(80)	11.556(2.098)
1.248	0.472(76)	0.501(85)	4.040(2.504)
1.620	0.134(278)	-0.008(213)	16.132(17.140)
1.802	0.208(161)	0.105(117)	3.924(6.088)
1.964	0.087(163)	0.022(114)	2.302(6.978)
2.128	0.097(384)	0.084(275)	-1.382(12.666)

TABLE VI: DWF results for C_5^A, C_6^A and $G_{\pi N\Delta}$ along with their Q^2-dependence shown in the first column. The errors quoted are jackknife statistical errors.